Hyaloperonospora arabidopsidis ATR1 effector is a repeat protein with distributed recognition surfaces

Seemay Chou[a,1], Ksenia V. Krasileva[b,1], James M. Holton[c,d], Adam D. Steinbrenner[b], Tom Alber[a,2], and Brian J. Staskawicz[b,2]

Departments of [a]Cell and Molecular Biology and [b]Plant and Microbial Biology, University of California, Berkeley, CA 94720; [c]Department of Biochemistry and Biophysics, University of California, San Francisco, CA 94158; and [d]Advanced Light Source, Lawrence Berkeley National Laboratory, Berkeley, CA 94720

Contributed by Brian J. Staskawicz, June 17, 2011 (sent for review April 14, 2011)

The *in planta* association of the *Hyaloperonospora arabidopsidis* effector ATR1 with the cognate *Arabidopsis thaliana* RPP1 immune receptor activates a disease-resistance signaling pathway that inhibits its pathogen growth. To define the molecular events specifying effector recognition by RPP1, we determined the crystal structure of ATR1 and assayed *in planta* the effects of surface polymorphisms that are critical to activating plant immunity. ATR1 adopts an elongated, all-helical, two-domain, seahorse-like structure with an overall architecture unlike any previously described fold. Structural comparisons highlight a tandemly duplicated, five-helix motif in the C-terminal domain that creates a structural framework for rapid diversification. Identification and mapping of critical recognition sites suggest that ATR1 detection by the RPP1 resistance protein is mediated by several distinct protein surfaces that allow the effectors to escape recognition through diverse surface polymorphisms. ATR1 gain-of-recognition mutants demonstrate that multiple amino acid substitutions are necessary for recognition and that surface polymorphisms exert additive effects. These results suggest that ATR1 is a modular repeat protein belonging to an ancient family of oomycete effectors that rapidly evolves to escape host detection and adopt diverse virulence functions.

plant innate immunity | obligate biotroph

Oomycetes form a monophyletic group of organisms that morphologically resemble fungi but are evolutionarily more closely related to brown algae and *Alveolates* (1). Oomycetes include a variety of commercially important plant pathogens with a diverse range of hosts, such as *Phytophthora infestans,* which causes tomato and potato late blight, *Phytophthora sojae* (soybean stem and root rot), *Phytophthora ramorum* (sudden oak death), and *Plasmopara viticola* (grapevine downy mildew), as well as *Hyaloperonospora arabidopsidis (Hpa*; previously known as *Peronospora parasitica)*, a pathogen of the model plant *Arabidopsis thaliana*. Similar to many other plant and animal pathogens that deliver virulence effectors into the host to establish infection, oomycetes physically interact with their hosts through specialized haustorial feeding structures that facilitate the delivery of effector proteins into host cells, where they have intracellular targets and play critical roles in oomycete survival and growth (2). Despite substantial progress toward characterizing the roles of effectors, the unifying mechanisms by which oomycete effectors promote virulence remain largely unknown.

Oomycete effector genes have a number of conserved features. Although the mechanisms of effector translocation are not well understood, a typical eukaryotic signal sequence found in all effectors is thought to mediate secretion out of the pathogen. In most effectors, oomycete-specific RxLR and dEER motifs promote further translocation of effectors into the host cell (3–7). Recently, genome sequences of *Hpa* and *Phytophthora* species allowed identification of numerous genes containing the conserved N-terminal signal peptide and RxLR–dEER motifs (8, 9). A large superfamily of *Phytophthora* effectors contains conserved C-terminal W, Y, and/or L motifs that are often repeated in the protein (10).

The *Hpa*/*Arabidopsis* system has been adopted as a model system for studying plant–oomycete interactions. The *Hpa* genome encodes 135–150 putative RxLR-containing effectors (8, 9), including *A. thaliana* Recognized 1 (ATR1; ref. 11). During the course of coevolution, plants have developed surveillance systems dependent on highly polymorphic resistance proteins (R proteins). R proteins directly or indirectly detect pathogen-derived effector molecules (12–14) to induce a cascade of immune responses that are collectively known as effector-triggered immunity (ETI; refs. 15 and 16). The hallmark of ETI responses is localized cell death, called the hypersensitive response (HR). Thus, pathogen effectors such as ATR1 have dual effects in promoting pathogen growth yet mediating recognition by the plant immune system through R proteins.

Several dozen *Arabidopsis* R genes, including Recognition of Peronospora Parasitica 1 (RPP1), confer resistance to *Hpa* (11, 17, 18). RPP1, through its polymorphic leucine-rich repeat (LRR) domain, associates with ATR1 variants, leading to activation of plant disease resistance (17), This model of direct, physical interactions between ATR1 and RPP1 is supported by the apparent positive selection for sequence polymorphisms in both ATR1 and RPP1 (11, 18). Moreover, only specific pairs of ATR1 and RPP1 alleles mediate recognition and immunity (11), suggesting a form of immune response in plants that evolves rapidly to adapt to the cognate pathogen.

To explore the basis for ATR1 recognition by RPP1 and the mechanisms by which ATR1 mutations mediate escape from the host HR, we determined the crystal structure of ATR1 at 2.3-Å resolution. ATR1 is a monomeric, modular protein with two structural domains comprised of α-helices. Two structurally similar five-helical repeats that display no sequence homology to each other form the C-terminal domain. Deletion analysis shows that segments of both structural domains are required for recognition of ATR1 by RPP1. Naturally occurring polymorphisms of ATR1 allowed identification of surface residues critical for recognition. Multiple polymorphisms are needed to switch the specificity of ATR1 alleles, and the differential effects of mutations show that different alleles of RPP1 may recognize distinct surfaces of ATR1. Our results show that ATR1 belongs to an ancient family of conserved oomycete effectors that evolves rapidly through surface polymorphisms to escape host recognition while maintaining a conserved structural core.

Author contributions: S.C., K.V.K., J.M.H., A.D.S., T.A., and B.J.S. designed research; S.C., K.V.K., and A.D.S. performed research; K.V.K. contributed new reagents/analytic tools; S.C., K.V.K., J.M.H., A.D.S., T.A., and B.J.S. analyzed data; and S.C., K.V.K., A.D.S., T.A., and B.J.S. wrote the paper.

The authors declare no conflict of interest.

Freely available online through the PNAS open access option.

Data deposition: The atomic coordinates have been deposited in the Protein Data Bank, www.pdb.org (PDB ID code 3RMR).

[1]S.C. and K.K. contributed equally to this work.

[2]To whom correspondence may be addressed. E-mail: stask@berkeley.edu or tom@ucxray.berkeley.edu.

This article contains supporting information online at www.pnas.org/lookup/suppl/doi:10.1073/pnas.1109791108/-/DCSupplemental.

Results

ATR1 Structure. To determine the ATR1 structure, several protein variants were expressed and purified from *Escherichia coli*. ATR1Δ15, which included the RXLR/dEER translocation motif, expressed but was not amenable to crystallization. Focusing on the effector domain sufficient for recognition by RPP1, we determined the crystal structure of ATR1Δ51 (Fig. 1*A*) from *Hpa* Emoy2 at 2.3-Å resolution. Initial phases were generated by multiwavelength anomalous diffraction, and the model was refined to R/R_{free} values of 0.2231/0.2598 (Table S1). Three copies of ATR1Δ51 crystallized in the asymmetric unit (AU). The three molecules in the AU are similar, with a Cα root-mean-square deviation (RMSD) of 0.43 Å. No clear electron density was obtained for the N terminus (residues 51–62 of chain A, 51–62 of chain B, and 51–66 of chain C) and a loop connecting α12 and α13 (residues 278–290 of chain A, 280–289 of chain B, and 282–289 of chain C).

ATR1 adopts a two-domain, extended, seahorse-like structure comprising 13 α-helices (Fig. 1*B*). The N-terminal head (α1–α3) forms a three-helix bundle separated from the larger C-terminal body (α4–α13) by a loop, or neck region (amino acid residues 117–126). The neck contains two β-turns, as well as several hydrogen bonds between Leu-118 and Tyr-126; Gly-120 and His-123; His-123 and Thr-125; and Asp-124 and Asp-127 (Fig. S1). Analysis of the electrostatic surface potential of ATR1 reveals numerous distributed positively and negatively charged patches, including a major region of positive potential on the head and two major negatively charged regions on the body (Fig. S2). Mapping the sequence conservation among ATR1 alleles shows that polymorphic residues are distributed across the surface of the head, neck, and body (Fig. S3). Hydrophobic and aromatic patches occur on the exposed surfaces of helices α2 and α3 in the head domain, as well as a C-terminal pocket in the groove between helices α11, α12, and α13 containing six Phe or Tyr residues. The first ordered residues in the structure, Trp–Pro–Phe-63–65, are unusually exposed for such hydrophobic amino acids.

Comparison of the entire ATR1 effector domain with available structures using the DALI server (19) did not reveal any significant structural homologs. Separate analysis of the N-terminal head and C-terminal body identified several potential distant homologs, with the circadian regulator KaiA [Protein Data Base (PDB) ID 1R5Q] giving the best match (Z score = 5.8) to an X-type, four-helix-bundle segment (Fig. S4*A*). ATR1 α5–α8 aligns with four helices of KaiA (residues 13–91) with RMSD of 2.7 Å. However, the electrostatic surfaces of the aligned structures are distinct. ATR1 also has a more extended loop between α5 and α6, and the KaiA helices analogous to ATR1 α7 and α8 are longer (Fig. S4*A*). To test the putative role of ATR1 in clock regulation, we measured *Arabidopsis* circadian rhythms via the TOC1:LUC reporter (*SI Materials and Methods*) in the absence and presence of ATR1. ATR1 had no effect on the transcriptional control of the circadian clock (Fig. S4 *B*–*D*).

The C-terminal body domain of ATR1 contains a structural repeat that is not evident in the sequence. Helices α4–α8 (residues 126–208) form a five-helix subdomain that resembles the next five-helix segment (α9–α13, residues 212–311; Cα RMSD = 5.1 Å; Fig. 2*B*). This ATR1 structural repeat comprises a capping helix crossing the first two helices of an X-type, antiparallel four-helix bundle. The arrangement of helices α4–α6 is particularly similar to α9–α11 (Cα RMSD = 3.2 Å). The fourth and fifth helices of the two repeats are not only more structurally variable, but they also are connected by the longest loops (11 and 19 residues, respectively) in the repeats. Because the first helix in the first ATR1 repeat is nearly parallel to the first helix in the second repeat, the variable loops fall on the same side of the elongated structure. A structure-based sequence alignment shows only 4% identical residues (Fig. 2*D*), making this homology undetectable by amino acid sequence comparisons.

ATR1 Is a Monomer in Vitro and in Vivo. ATR1 packed in the crystals as two equivalent dimers with one formed by a crystallographic twofold rotation axis and the other formed by a noncrystallographic twofold. To determine whether this dimer reflects solution properties of ATR1, we analyzed the oligomerization state of recombinant protein in solution using size-exclusion chromatography. At 1 mg/mL (28 μM) in neutral pH buffer, ATR1 eluted at a volume corresponding to 30.2 kDa, similar to the molecular mass of a monomer, 29.5kDa (Fig. S5*A*).

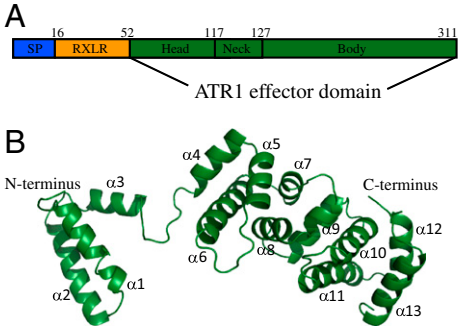

Fig. 1. The structure of the effector segment of ATR1. (*A*) A schematic representation of the domain architecture of ATR1. (*B*) Ribbon diagram showing the overall structure of the ATR1Δ51. Thirteen α-helices form N-terminal (α1–α3) and C-terminal (α4–α13) domains. The elongated structure is >80 Å across, significantly more extended than a globular protein of the same molecular mass.

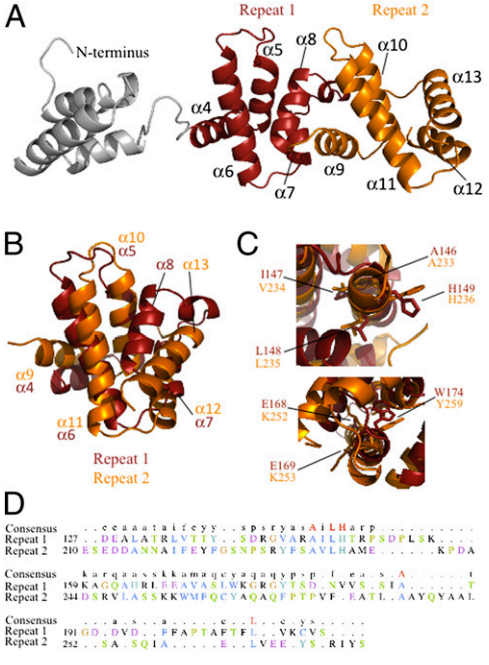

Fig. 2. A structural repeat in ATR1. (*A*) The C-terminal body domain of ATR1 contains two five-helix repeats with similar folds (orange and red). The ATR1 repeats are related primarily by a translation and a small rotation. (*B*) Structural alignment based on the second helix in each repeat (α5 and α10 aligned using PyMol) shows the similar helix arrangement with variable connecting loops. (*C*) The structural alignment reveals conserved residues in helix 2 (*Upper*) and similar residues in helix 3 (*Lower*) of the repeats. (*D*) Structure-based sequence alignment between the ATR1 repeats shows low sequence identity.

To test ATR1 stoichiometry in vivo, we performed coimmunprecipitations using FLAG- and HA-tagged ATR1 transiently expressed in *Nicotiana tabacum*. We used HA-tagged LRR of RPP1 as a positive control, as it has been shown to interact with ATR1 (10). FLAG-ATR1 was coexpressed with either HA-ATR1 or HA-LRR and immunoprecipitated by using anti-FLAG M2 Sepharose. HA-ATR1 failed to coimmunoprecipitate with FLAG-ATR1, showing that ATR1 does not form homo-oligomers in vivo (Fig. S5*B*).

Minimal ATR1 Region Recognized by RPP1–WsB Includes Parts of at Least Two Domains. To elucidate the structural basis of ATR1 recognition by the host, we used deletion analysis of ATR1–Emoy2 to define the minimal region recognized by RPP1. We introduced deletion endpoints based on ATR1 secondary structure (Fig. 3 *A* and *B*) and assayed their activity by transient coexpression with RPP1–WsB in *N. tabacum* (Fig. 3*C*). The localized cell death due to the HR was used as a marker for activation of RPP1-mediated defense responses. Deletions in ATR1Δ51 preserving or removing helix α1 (Δ67 and Δ87, respectively) did not affect activation of RPP1 but reduced ATR1 protein stability (Fig. 3*D*). Further N-terminal deletions failed to induce RPP1-dependent HR. Deletion of the C-terminal 90 amino acids compromised protein stability but did not affect recognition, suggesting that residues 87–222 are sufficient for RPP1 recognition. Further C-terminal deletions resulted in loss of HR (Fig. 3*C*), which may have been due to lower protein stability or removal of critical amino acids. The minimal recognition region comprising amino acids 87–222 includes helices α2–α3 in the ATR1 N-terminal head and the first five-helix repeat (residues 127–210) in the C-terminal body (Fig. 3*B*).

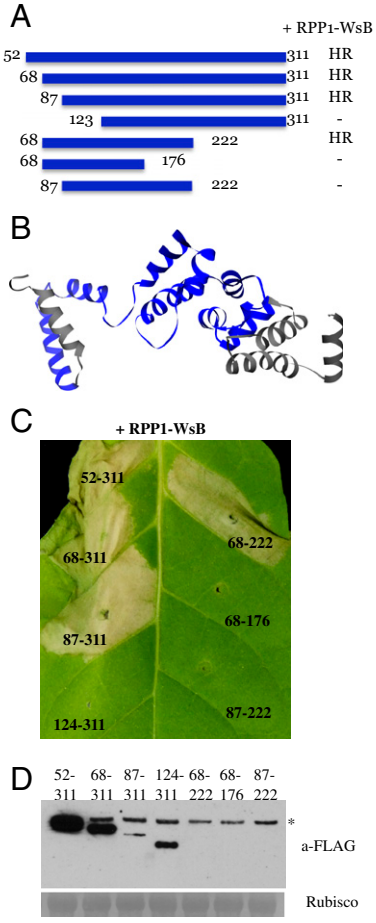

Fig. 3. *In planta* deletion analysis of ATR1–Emoy2. (*A*) Schematic diagram of deletion constructs and a summary of the HR phenotype. (*B*) Ribbon diagram showing the minimum recognition region (blue) of ATR1 containing the groove surrounding the neck and the first half of the C-terminal body domain. (*C*) Coinoculation of ATR1 truncations together with RPP1–WsB in *N. tabacum* showing the induction of RPP1-dependent HR. Fragments starting at residue 87 or ending at residue 222 are sufficient to induce the HR. (*D*) Western blot showing relative protein levels of the truncated ATR1 variants. Asterisk marks a nonspecific ~33-kDa band cross-hybridizing with anti-FLAG antibody. The C-terminal domain (residues 124–311) expresses and accumulates, but it does not trigger the HR. The 87–222 fragment encompassing the minimal recognition region is unstable.

Distinct ATR1 Residues Specify Recognition by Different RPP1 Alleles. We have previously used the natural polymorphisms between ATR1–Emoy2 and ATR1–Maks9 to identify two key residues that specify ATR1-dependent activation of RPP1–NdA (17). Here we followed a similar approach using the natural polymorphisms to define key amino acids that specify differential recognition of ATR1–Emoy2 and ATR1–Cala2 by RPP1–WsB. ATR1–Emoy2 and ATR1–Cala2 differ in 69 amino acid sites (Table S2), many of which are located in the C-terminal region of the protein. Because our deletion analysis identified the minimum region of ATR1 sufficient for recognition, we focused on polymorphisms located within this region (residues 87–222), restricting our analysis to 26 out of the 69 total polymorphisms. We further refined our analysis by looking for polymorphic sites that cosegregated between three ATR1 alleles recognized by RPP1–WsB (Emoy2, Maks9, Emco5) and two unrecognized alleles (Cala2 and Emwa1), yielding 14 sites that fulfilled these criteria (Fig. 4*A*).

We individually mutated these sites in ATR1–Cala2 and assessed their relative contributions to activation of RPP1–NdA and RPP1–WsB in *N. tabacum* (Fig. 4 and Fig. S6*A*). Substitutions at four sites produced gain-of-recognition phenotypes with RPP1–WsB that ranged from very mild (Asn-158–Lys) to intermediate (Val-122–Leu, Ser-125–Thr) to strong (Tyr-140–Asp; Fig. 4*B*). Combining the mutations had additive effects, and the quadruple ATR1–Cala2 mutant (Val-122–Leu/Ser-125–Thr/Tyr-140–Asp/Asn-158–Lys) induced HR with timing and intensity similar to wild-type ATR1–Emoy2 (Fig. 4*B*, Movie S1, and Fig. S7). Interestingly, activation of RPP1–NdA was not affected by any of these mutations (Fig. S6*A*). The reciprocal quadruple substitution in ATR1–Emoy2 significantly delayed activation of RPP1–WsB (Fig. S6*B*), suggesting that although these four residues are sufficient to switch specificity, there are likely to be additional interaction sites. These ATR1 variants expressed to the same levels (Fig. S6*C*), indicating that the changes in recognition specificity were not due to differences in protein stability.

Mapping these polymorphisms onto the structure of ATR1 shows that they all are surface-exposed, except Asp-140, which is partially buried (Fig. 4*C*). Most interestingly, the key ATR1 residues that are important for activation of RPP1–WsB versus RPP1–NdA are located on distinct protein surfaces. This finding indicates that variable RPP1 alleles are capable of recognizing different unrelated surface "epitopes" of ATR1.

Discussion

Although considerable progress has been made toward dissecting the molecular mechanisms underlying effector recognition by R proteins and the structural basis for HR activation, virulence functions for many effectors remain elusive. Oomycete and fungal effectors have been shown to evolve under strong positive selection that drives rapid divergence, making it difficult to detect effector homologs outside their genus using amino acid sequence comparisons or secondary-structure prediction tools. The 3D structure of the *Hpa* effector ATR1 differs from that of other effector proteins, including AvrL567-A and AvrL567-D,

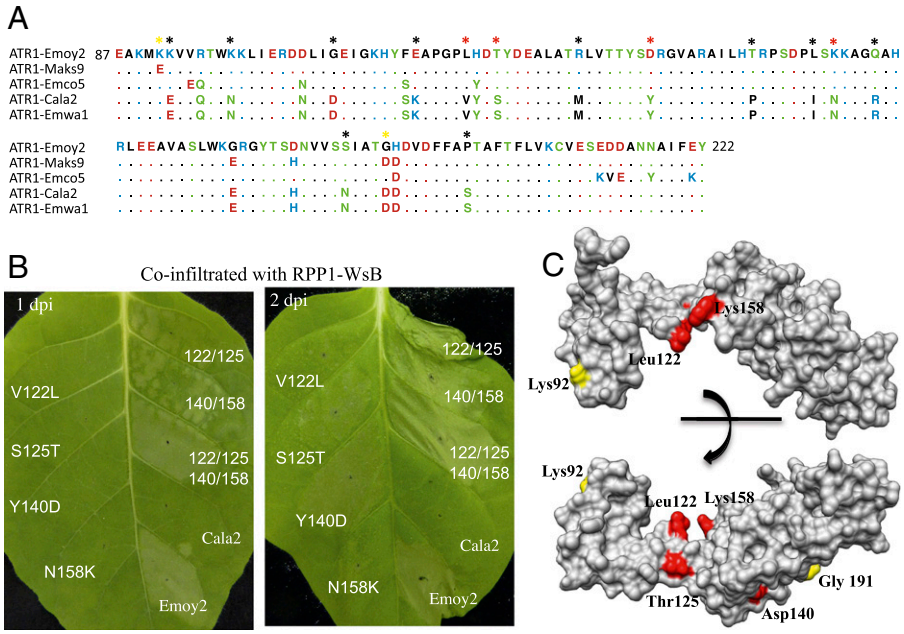

Fig. 4. Distributed surfaces contribute to RPP1 activation by ATR1. (*A*) Multiple sequence alignment of amino acids 87–222 of five ATR1 alleles. Previously identified amino acids critical for ATR1–Emoy2 recognition by RPP1–NdA (17) are marked with yellow asterisks. Residues that cosegregate with recognition of ATR1 by RPP1–WsB are shown with black asterisks. The four positions identified as individually critical for switching the specificity of HR activation are marked with red asterisks. (*B*) Additive effect of the four amino acids that contribute to recognition of ATR1 by RPP1–WsB as assayed by timing and intensity of HR in *N. tabacum*. The variants include: 122, ATR1–Cala2, Val-122–Leu; 125, ATR1–Cala2, Ser-125–Thr, 140, ATR1–Cala2, Tyr-140–Asp; 158, ATR1–Cala2, Asn-158–Lys; and combinations of these substitutions, as well as a wild-type ATR1–Cala2 (negative control) and wild-type ATR1–Emoy2 (positive control). (*C*) Surface representation of ATR1 with mapped polymorphisms, highlighting previously identified residues that were critical for recognition of ATR1 by RPP1–NdA (yellow) and our data revealing that recognition by RPP1–WsB relies on different critical sites (red).

two effectors from *Melampsora lini* (flax rust) differentially recognized by a cognate R protein L (20), and *Pseudomonas syringae* effectors AvrPto and AvrB (21, 22).

ATR1 folds into an elongated structure composed of two major helical domains connected by a linker containing several hydrogen bonds. The C-terminal domain is formed by an extended, right-handed solenoid of 10 helices that form two 5-helix repeats. This ATR1 structural repeat differs from previously defined helical repeat motifs. The ankyrin and tetratrichopeptide repeats, for example, form pairs of nearly antiparallel helices packed together in curved arcs (23). Similarly, the helices in HEAT and 14-3-3 repeats are longer and more nearly antiparallel, and these repeat arrays form curved architectures, rather than the straighter arrangement of the tandem ATR1 repeats. The clathrin repeat (24) forms a straight elongated structure like ATR1, but the clathrin helices are shorter, and they cross each other in a more regular, nearly antiparallel pattern.

The lack of significant sequence identity between the ATR1 repeats raises the question of whether these are genuine repeat sequences that arose by duplication and divergence. We note that many well-established helical repeat sequences show low pairwise sequence identity, and many motifs are recognizable only because they occur in tandem arrays. Similarly, most members of the superfamily of *Phytophthora* effectors containing W, Y, or L motifs show low pairwise sequence identity. Consequently, the tandem arrangement and structural similarity of the ATR1 repeats support the conclusion that this motif represents a previously undescribed helical repeat that is likely to be found not only in ATR1, but also in other proteins.

Sequence-based searches for proteins with structural similarity to ATR1 did not yield significant matches, although several putative homologs were found by searching for 3D structures similar to individual ATR1 segments. The highest-scoring structural homolog was KaiA, a cyanobacteria *Anabaena* sp. PCC7120 circadian clock protein (25) that aligned with ATR1 helices α4–α7. In light of this putative homology and the previously characterized link between circadian regulation and plant immune defense (26), we tested the role of ATR1 in circadian regulation. The presence of ATR1, however, does not significantly alter transcriptional regulation of *Arabidopsis* circadian rhythms. Given that this domain of KaiA is involved in promoting the kinase activity of its interacting partner KaiC, however, it is possible that the analogous region in ATR1 performs a similar biochemical function but a different physiological function. Other lower-scoring homologs include an RNA-binding protein RBP8 (aligns with α4–α9) and Skp1 (aligns with α4–α10), an adaptor protein in the human SCF E3 ubiquitin–ligase complex. These structural similarities may offer initial insights into biochemical functions and potential partners of ATR1.

Although dimerization of R proteins appears to be required to activate immune responses (17, 27) and several other fungal and bacterial effectors function as dimers (28), ATR1 behaves as a monomer in vivo and in vitro. These results suggest that ATR1 does not serve as dimerization platform for RPP1. However, our results do not exclude the possibility that ATR1 may oligomerize in complex with RPP1 or other host partners.

ATR1–Emoy2 recognition by RPP1–NdA relies on two polymorphic sites in *Hpa* strains—Lys-92 and Gly-191 (17). These sites lie on opposite sides of the ATR1 structure in two different domains, suggesting that both positions can function in recognition. Unexpectedly, three of four natural ATR1 variations (amino acids 122, 125, and 158) associated with recognition by another allele, RPP1–WsB, occur on a different surface of the protein. In contrast, a fourth RPP1–WsB selective residue that we identified (Asp-140) occurs on the same surface as Gly-191, which promotes activation through RPP1–NdA (17). This difference in the basis for activation specificity of Rpp1–WSB and RPP1–NdA supports the idea that RPP1 directly recognizes

ATR1 and suggests that these RPP1 alleles recognize distinct surface epitopes of ATR1. The existence of RPP1 alleles capable of recognizing different protein surfaces of ATR1 suggests that LRRs play a versatile role in plant immunity.

The additive effects of the ATR1 polymorphisms suggest that R-protein activation is more complicated than a simple on/off switch. Most likely, the response kinetics are controlled by different binding affinity of ATR1 variants, which can affect the release of negative regulation through either inter- or intramolecular interactions and/or nucleotide binding activity of the NBS domain of RPP1. Defining the mechanisms that control kinetics of R-protein activation is the next critical step in understanding initiation of plant defense responses and plant cell death.

Our mutational analysis of ATR1 reveals that RPP1 exhibits rapidly evolving recognition of different ATR1 protein surfaces. This finding suggests that recognition of each effector could have evolved independently in closely related plant lineages. Changes in plant immune receptors happen in the germ line; thus, plant immunity is innate. Therefore, R proteins, such as RPP1, that rapidly gain new recognition specificities provide an adaptive advantage to plant species on the population level. Interpreting ATR1 polymorphisms in the context of the ATR1 structure provides a framework for understanding how pathogens may escape detection and how plant hosts evolve to maintain effector recognition. Further understanding of the molecular mechanisms that allow R proteins to respond to effectors could lead to engineering optimized plant pathogen receptors—potentially powerful new tools to contain some of the most important plant pathogens.

Materials and Methods

Strains and Growth Conditions. Bacterial DNA transformation was conducted by using chemically competent *E. coli* DH5a (Invitrogen), electroporation of *E. coli* Rosetta (DE3), or through freeze/thaw transformation of $CaCl_2$-competent *A. tumefaciens* (29). *N. tabacum* (variety Turk), and *A. thaliana* plants were grown in a controlled growth chamber at 24 °C at 16-h light/8-h dark photoperiod before infiltrations and switched to 24-h light after infiltrations.

ATR1 Cloning, Protein Expression, and Purification. The ATR1Δ51 Emoy2 deletion variant (17) was cloned into the pDUET vector (Addgene) after adding BamHI/NotI sites and a cleavage site for Tobacco Etch Virus (TEV) protease to the 5′ and 3′ ends of ATR1 through PCR amplification. For $(His)_6$-ATR1Δ51 protein expression, the pDUET construct was transformed into *E. coli* Rosetta (DE3; Novagen), cells were grown at 37 °C to OD_{600} = 0.7–0.8, and induced with 0.5 mM isopropyl β-D-1-thiogalactopyranoside for 6–8 h at 18 °C. The cells were harvested by centrifugation for 15 min at 5,000 × g at 4 °C and frozen in liquid nitrogen for storage at −20 °C before purification.

Cells were resuspended in Ni-A Buffer [20 mM Hepes, pH 7.5, 0.5 M NaCl, 0.5 mM Tris-(2-carboxyethyl)phosphine (TCEP), 25 mM imidazole, 10% glycerol, 0.2 mM 4-(2-aminoethyl)-benzenesulfonyl fluoride (AEBSF)] and 4-(2-Aminoethyl) benzenesulfonyl fluoride hydrochloride lysed by sonication. The lysate was centrifuged for 1 h at 20,000 × g (4 °C), and the supernatant was passed over a Ni affinity column (GE). $(His)_6$-ATR1Δ51 was recovered by gradient elution with Ni-B Buffer (20 mM Hepes, pH 7.5, 0.5 M NaCl, 0.5 mM TCEP, 350 mM imidazole, 10% glycerol, 0.2 mM AEBSF) using the AKTA Explorer FPLC system (GE). Fractions containing $(His)_6$-ATR1Δ51 were verified by SDS/PAGE and pooled for tag cleavage for 22 h at 4 °C with 1:50 TEV protease. Untagged ATR1Δ51 was loaded on a Superdex S75 gel filtration column (GE) and eluted as a monomer in 20 mM Hepes (pH 7.5), 100 mM NaCl, and 0.5 mM TCEP. The protein was concentrated to 20 mg/mL.

Structure Determination and Analysis. Preliminary ATR1Δ51 crystals were obtained by hanging drop vapor diffusion trials at 18 °C from a 2:1 mixture of 20 mg/mL protein with 0.1 M Mes (pH 6.5) and 1.6 M $MgSO_4$. Diffraction-quality crystals were obtained by hanging drop vapor diffusion at 18 °C by seeding at 1:20,000 into a 4:1 mixture of ATR1Δ51 at 15 mg/mL with 0.1 M Mes (pH 5.0), 1.2 M $MgSO_4$, and 0.01% acetonitrile for 3–4 d. Crystals dehydrated by transfer to a 0.1 M Mes (pH 5.0) and 1.5 M $MgSO_4$ solution for 2 h at 18 °C were immersed in mother liquor containing 14% ethylene glycol, mounted, and flash frozen in liquid N_2. Diffraction data were collected at the Lawrence Berkeley National Laboratory Advanced Light Source Beamline 8.3.1 (30). Data reduction and initial maps were obtained by using the automated ELVES program (31). Phases were obtained experimentally with data from selenomethionine-substituted ATR1Δ51. The PHENIX software suite was used for initial model building. The final model was built by iterative manual model building using Coot (32) and maximum likelihood refinement with PHENIX (33). Structure was validated by using MOLProbity (34). Images and structural alignments were generated by using PyMol (35) and Chimera (36). Multiple sequence alignment of the five ATR1 alleles was done by using the MUSCLE algorithm (37) and visualized in CLC Genomics Workbench (CLC bio). Structure comparisons were done by using the DALI server (19) and Chimera (36). Coordinates and structure factors were deposited in the PDB (PDB ID: 3RMR).

Functional Analysis of ATR1 in *N. tabacum*. Deletions in ATR1Δ51 pENTRY/TOPO (17) were made through PCR amplification. The resulting products were introduced in pENTRY/TOPO (Invitrogen) and subsequently into pEG202 (35S promoter, N-terminal FLAG tag fusion; ref. 37) by using LR clonase (Invitrogen). Site-directed mutants were made in ATR1 pENTRY/TOPO by using the Quick-Change SDM Kit (Stratagene) and subsequently introduced into pEG202. *Agrobacterium*-mediated transient expression in *N. tabacum* was performed as described (17). Protein expression was sampled at 24–48 h after induction and assayed as described (17).

ACKNOWLEDGMENTS. We thank Doug Barrick, Terry Lang, Sophien Kamoun, and Mark Banfield for helpful discussions; Bryan Thines and Frank Harmon (both of the Plant Gene Expression Center, U.S. Department of Agriculture) for providing *Arabidopsis* TOC1:LUC seed and guiding us in circadian clock experiments; Jane Tanamachi and George Meigs at Advanced Light Source Beamline 8.3.1 for help with X-ray data collection; Nathaniel Echols for help with model building of the ATR1 structure; and Sandra Goritschnig, Daniil Prigozhin, Megan Casey, and Christoph Grundner for helpful comments and support. This project was supported by National Science Foundation Grant NSF 2010 0726229.

1. Göker M, Voglmayr H, Riethmüller A, Oberwinkler F (2007) How do obligate parasites evolve? A multi-gene phylogenetic analysis of downy mildews. *Fungal Genet Biol* 44: 105–122.
2. Dodds PN, et al. (2009) Effectors of biotrophic fungi and oomycetes: Pathogenicity factors and triggers of host resistance. *New Phytol* 183:993–1000.
3. Bhattacharjee S, et al. (2006) The malarial host-targeting signal is conserved in the Irish potato famine pathogen. *PLoS Pathog* 2:e50.
4. Dou D, et al. (2008) Conserved C-terminal motifs required for avirulence and suppression of cell death by Phytophthora sojae effector Avr1b. *Plant Cell* 20:1118–1133.
5. Grouffaud S, van West P, Avrova AO, Birch PRJ, Whisson SC (2008) Plasmodium falciparum and Hyaloperonospora parasitica effector translocation motifs are functional in Phytophthora infestans. *Microbiology* 154:3743–3751.
6. Whisson SC, et al. (2007) A translocation signal for delivery of oomycete effector proteins into host plant cells. *Nature* 450:115–118.
7. Bailey K, et al. (2011) Molecular cloning of ATR5Emoy2 from Hyaloperonospora arabidopsidis, an avirulence determinant that triggers RPP5-mediated defense in Arabidopsis. *Mol Plant Microbe Interact* 24:827–838.
8. Win J, et al. (2007) Adaptive evolution has targeted the C-terminal domain of the RXLR effectors of plant pathogenic oomycetes. *Plant Cell* 19:2349–2369.
9. Baxter L, et al. (2010) Signatures of adaptation to obligate biotrophy in the Hyaloperonospora arabidopsidis genome. *Science* 330:1549–1551.
10. Jiang RHY, Tripathy S, Govers F, Tyler BM (2008) RXLR effector reservoir in two Phytophthora species is dominated by a single rapidly evolving superfamily with more than 700 members. *Proc Natl Acad Sci USA* 105:4874–4879.
11. Rehmany AP, et al. (2005) Differential recognition of highly divergent downy mildew avirulence gene alleles by RPP1 resistance genes from two Arabidopsis lines. *Plant Cell* 17:1839–1850.
12. Jia Y, McAdams SA, Bryan GT, Hershey HP, Valent B (2000) Direct interaction of resistance gene and avirulence gene products confers rice blast resistance. *EMBO Journal* 19:4004–4014.
13. Shao F, et al. (2003) Cleavage of Arabidopsis PBS1 by a bacterial type III effector. *Science* 301:1230–1233.
14. Andersson MX, Kourtchenko O, Dangl JL, Mackey D, Ellerström M (2006) Phospholipase-dependent signalling during the AvrRpm1- and AvrRpt2-induced disease resistance responses in Arabidopsis thaliana. *Plant J* 47:947–959.
15. Chisholm ST, Coaker G, Day B, Staskawicz BJ (2006) Host-microbe interactions: Shaping the evolution of the plant immune response. *Cell* 124:803–814.
16. Jones JDG, Dangl JL (2006) The plant immune system. *Nature* 444:323–329.
17. Krasileva KV, Dahlbeck D, Staskawicz BJ (2010) Activation of an Arabidopsis resistance protein is specified by the in planta association of its leucine-rich repeat domain with the cognate oomycete effector. *Plant Cell* 22:2444–2458.

18. Botella MA, et al. (1998) Three genes of the Arabidopsis RPP1 complex resistance locus recognize distinct Peronospora parasitica avirulence determinants. *Plant Cell* 10:1847–1860.
19. Holm L, Rosenstrom P (2010) Dali server: Conservation mapping in 3D. *Nucleic Acids Res* 38:W545–W549.
20. Wang C-IA, et al. (2007) Crystal structures of flax rust avirulence proteins AvrL567-A and -D reveal details of the structural basis for flax disease resistance specificity. *Plant Cell* 19:2898–2912.
21. Dong J, et al. (2009) Crystal structure of the complex between Pseudomonas effector AvrPtoB and the tomato Pto kinase reveals both a shared and a unique interface compared with AvrPto-Pto. *Plant Cell* 21:1846–1859.
22. Lee CC, et al. (2004) Crystal structure of the type III effector AvrB from Pseudomonas syringae. *Structure* 12:487–494.
23. Gardino AK, Smerdon SJ, Yaffe MB (2006) Structural determinants of 14-3-3 binding specificities and regulation of subcellular localization of 14-3-3-ligand complexes: A comparison of the X-ray crystal structures of all human 14-3-3 isoforms. *Semin Cancer Biol* 16:173–182.
24. Ybe JA, et al. (1999) Clathrin self-assembly is mediated by a tandemly repeated superhelix. *Nature* 399:371–375.
25. Williams SB, Vakonakis I, Golden SS, LiWang AC (2002) Structure and function from the circadian clock protein KaiA of Synechococcus elongatus: A potential clock input mechanism. *Proc Natl Acad Sci USA* 99:15357–15362.
26. Wang W, et al. (2011) Timing of plant immune responses by a central circadian regulator. *Nature* 470:110–114.
27. Bernoux M, et al. (2011) Structural and functional analysis of a plant resistance protein TIR domain reveals interfaces for self-association, signaling, and autoregulation. *Cell Host Microbe* 9:200–211.
28. Catanzariti A-M, et al. (2010) The AvrM effector from flax rust has a structured C-terminal domain and interacts directly with the M resistance protein. *Mol Plant Microbe Interact* 23:49–57.
29. Wise AA, Liu Z, Binns AN (2006) Three methods for the introduction of foreign DNA into Agrobacterium. *Methods Mol Biol* 343:43–53.
30. MacDowell AA, et al. (2004) Suite of three protein crystallography beamlines with single superconducting bend magnet as the source. *J Synchrotron Radiat* 11: 447–455.
31. Holton J, Alber T (2004) Automated protein crystal structure determination using ELVES. *Proc Natl Acad Sci USA* 101:1537–1542.
32. Emsley P, Cowtan K (2004) Coot: Model-building tools for molecular graphics. *Acta Crystallogr D Biol Crystallogr* 60:2126–2132.
33. Adams PD, et al. (2010) PHENIX: A comprehensive Python-based system for macromolecular structure solution. *Acta Crystallogr D Biol Crystallogr* 66:213–221.
34. Davis IW, Murray LW, Richardson JS, Richardson DC (2004) MOLPROBITY: Structure validation and all-atom contact analysis for nucleic acids and their complexes. *Nucleic Acids Res* 32:W615–W619.
35. Shindyalov IN, Bourne PE (1998) Protein structure alignment by incremental combinatorial extension (CE) of the optimal path. *Protein Eng* 11:739–747.
36. Pettersen EF, et al. (2004) UCSF Chimera—a visualization system for exploratory research and analysis. *J Comput Chem* 25:1605–1612.
37. Edgar R (2004) MUSCLE: Multiple sequence alignment with high accuracy and high throughput. *Nucleic Acids Res* 19:1792–1797.
38. Earley KW, et al. (2006) Gateway-compatible vectors for plant functional genomics and proteomics. *Plant J* 45:616–629.